Research Article | Vol. 29, No. 17 / 16 Aug 2021 / Optics Express 27416
Optics EXPRESS

# Study of wavelength-dependent pulse self-compression for high intensity pulse propagation in gas-filled capillaries

GARIMA C. NAGAR[1,2] AND BONGGU SHIM[1,3]

[1]Department of Physics, Applied Physics, and Astronomy, Binghamton University, State University of New York, Binghamton, NY 13902, USA
[2]gnagar1@binghamton.edu
[3]bshim@binghamton.edu

**Abstract:** We theoretically investigate the wavelength-dependent pulse self-compression dynamics of intense femtosecond laser pulses in gas-filled capillaries. Simulations with $\lambda = 1, 2, 3$ and 4 μm using the multimode carrier-resolved unidirectional pulse propagation equation reveal pulse self-compression or pulse broadening depending on plasma and modal dispersion. Our study shows that the pulse at 1 μm exhibits better pulse self-compression compared with longer wavelengths due to smaller group velocity mismatch between fundamental and higher-order capillary modes.



## 1. Introduction

Gas-filled capillaries have provided an excellent and robust tool for demonstrating high-intensity nonlinear optics such as high-order harmonic generation (HHG) [1] due to their extended lengths and good mode profiles. Furthermore, they have been used for novel nonlinear optics experiments [2,3] such as demonstration of multidimensional soliton states [4–6], ultraviolet generation through soliton dynamics [7], and spatiotemporal mode-locked lasers [8].

In addition, gas-filled capillaries have been used for pulse compression. Self-phase modulation and/or rotational and vibrational Raman effects [9–15] induce spectral broadening, which is followed by post pulse compression schemes such as a pair of gratings or chirped mirrors [16–18]. However, these schemes are generally limited to lower intensities (i.e., below ionization threshold) and thus requires long capillaries. In contrast, pulse self-compression can occur above the gas ionization threshold due to plasma defocusing even in short (i.e., a few cm) capillaries and there have been various studies of pulse propagation and resulting pulse self-compression in gas-filled capillaries [19–25]. For instance, pulse self-compression by a factor of $\sim 2.3$ has been observed in low-pressure Ar filled capillary through ionization-induced spatio-temporal reshaping [20]. Recently, Gao *et al*. [25] have reported spatio-temporal localization in a multiply ionized Ar gas in capillaries and have also shown that UV wavelengths and smaller capillary radii are preferred for better mode confinement. However, to the best of our knowledge, there has been no systematic study or detailed analysis of wavelength-dependent pulse propagation in gas-filled capillaries, in particular, ionization-induced pulse self-compression with mid-infrared (IR) wavelengths in the weak ionization regime. Although pulse self-compression can also occur in laser filamentation that is self-guidance of a high power laser pulse [26–30], gas-filled capillaries are preferred over filamentation due to better mode quality and higher intensity [31].

In this Article, we numerically investigate the wavelength-dependent pulse self-compression dynamics during nonlinear pulse propagation in gas-filled capillaries spanning near and mid-IR for the weak ionization regime in which nonlinear optics experiments such as HHG are frequently performed. In particular, mid-IR pulses have received significant attention because of favorable scalability in nonlinear optics. For instance, the HHG cut-off scales with $\lambda^2$, where $\lambda$ is the driver

#432478 https://doi.org/10.1364/OE.432478
Journal © 2021 Received 25 May 2021; revised 30 Jul 2021; accepted 31 Jul 2021; published 10 Aug 2021

Optics EXPRESS

wavelength [1]. For laser filamentation [32–42], the power-contained in a single filament also scales with $\lambda^2$ so that higher powers can be transported in laser filaments with mid IR than near IR or visible light [43–52]. In our work, pulse propagation is modeled using the multimodal carrier-resolved unidirectional pulse propagation equation (UPPE) [53]. We investigate the nonlinear spatio-temporal dynamics of laser pulses via plasma and wavelength-dependent modal dispersion. We consider four laser wavelengths covering near and mid IR (1, 2, 3 and 4 μm). We find that plasma defocusing and rapid excitation of high-order transverse capillary modes produce complex spatio-temporal dynamics. In contrast to laser filamentation where pulse self-compression can be more efficient for long wavelengths [44], pulse self-compression in gas-filled capillaries due to plasma is more efficient for short wavelengths, for instance, compression by a factor of maximum 3.3 for $\lambda = 1$ μm. Our finding is explained by larger group velocity mismatch (GVM) between fundamental and higher-order modes at longer wavelengths. In addition, for pulse self-compression with long wavelengths, we find that large input pulse powers and capillary radii are required for long wavelengths to enhance self-focusing induced plasma effects and minimize GVM among different modes. Since long wavelengths are intensively studied and frequently used in many areas of laser matter-interactions, it is critical to understand the wavelength-dependent dynamics of nonlinear propagation.

## 2. Numerical simulations

We simulate the pulse propagation in gas-filled capillaries using the carrier-resolved, radially symmetric unidirectional pulse propagation (UPPE) including modal expansion in the transverse direction. The propagation equation to calculate the evolution of each modal component is written as [25,41,54–56]

$$\frac{\partial \widetilde{E_n}}{\partial z} = i[k_{z,n}(\omega) - \frac{\omega}{v_g} + i\beta_n]\widetilde{E_n} + \frac{i}{2k_{z,n}(\omega)}\frac{\omega^2}{c^2}\frac{\widetilde{P}_{NL,n}}{\epsilon_0} - \frac{1}{2k_{z,n}(\omega)}\frac{\omega}{c}\frac{\widetilde{J}_n}{\epsilon_0 c} - \frac{\widetilde{\alpha}_{NL,n}}{2}, \tag{1}$$

where the terms with ˜ represent the ones in the spectral domain. We decompose Fourier transform of the carrier-resolved electric field into the discrete modal components written as $\widetilde{E} = \sum_n \widetilde{E}_n J_0(\gamma_n r/a_0)$, where $J_0(\gamma_n r/a_0)$ is the normalized zeroth-order Bessel function with $\gamma_n$ being the $n^{th}$ root of $J_0$ and $a_0$ being the radius of the capillary. $k_{z,n} = \sqrt{k^2(\omega) - k_{\perp,n}^2}$ is the wave number in the propagation direction, where $k(\omega) = n(\omega)\omega/c$, $n(\omega)$ is the Ar refractive index [57], $\omega$ is the angular frequency, $c$ is the speed of light and $k_{\perp,n} = \gamma_n/a_0$. The propagation equation (Eq. (1)) is solved in the pulse frame moving with the group velocity of the fundamental mode ($v_g = (dk_{z,1}/d\omega\ |_{\omega=\omega_0})^{-1}$), where $\omega_0$ is the central frequency of the laser. Under the condition of $k(\omega_0)a_0 \gg \gamma_n$ [58], the loss coefficient is given by $\beta_n = [0.5(1 + n_e^2)/(n_e^2 - 1)^{1/2}](\gamma_n\lambda/2\pi)^2/a_0^3$, where $n_e$ is the refractive index of cladding. $\widetilde{P}_{NL,n}$ is the modal component [i.e., $\widetilde{P}_{NL} = \sum_n \widetilde{P}_{NL,n}J_0(\gamma_n r/a_0)$] of Fourier transform of the nonlinear polarization ($P_{NL}$) which is given by $P_{NL}(t) = \epsilon_0\chi^{(3)}E^3$. Here $\epsilon_0$ is the free space permittivity and $\chi^{(3)}$ is the third-order susceptibility. The ionization effects such as plasma defocusing and absorption are incorporated by calculating the free charge-induced current ($J$). $\widetilde{J}_n$ is the modal component [i.e., $\widetilde{J} = \sum_n \widetilde{J}_n J_0(\gamma_n r/a_0)$] of Fourier transform of $J$ which is given by $J(t) = (e^2/m_e)(\nu_e + i\omega)/(\nu_e^2 + \omega^2)\rho(t)E(t)$, where $m_e$ and $e$ are the electron mass and charge, respectively, $\nu_e$ is the electron collision frequency, and $\rho$ is the free electron density. $\widetilde{\alpha}_{NL,n}$ is the modal component [i.e., $\widetilde{\alpha}_{NL} = \sum_n \widetilde{\alpha}_{NL,n}J_0(\gamma_n r/a_0)$] of Fourier transform of the absorption due to optical field ionization ($\alpha_{NL}$), which is given by $\alpha_{NL}(t) = \frac{\rho_0 W(I)U}{I}E$, where $\rho_0$ is the neutral gas density, $W(I)$ is the optical field ionization (OFI) rate, $U$ is the ionization energy and $I$ is the intensity of the pulse.

In order to calculate free electron densities, Eq. (1) is coupled with the following plasma equation:

$$\frac{\partial \rho}{\partial t} = W(I)(\rho_0 - \rho) + \frac{\sigma_B I}{U}\rho, \tag{2}$$

Optics EXPRESS

where $\rho$ is the plasma density, $W(I)$ is the OFI rate by the Perelemov-Popov-Terentev (PPT) ionization model [59], $\sigma_B = \omega_0^2\tau_c/[n(\omega_0)c\rho_c(1+\omega_0^2\tau_c^2)]$ is the cross section for collisional ionization, where $\tau_c$ is the electron collision time and $\rho_c$ is the critical plasma density for the driver laser.

We use 5-cm long Ar-filled capillaries [1] with 1 bar pressure in our simulations. For our simulation parameters, various temporal phenomena such as pulse self-compression, pulse splitting, etc. are clearly observed within the 5-cm propagation distance. The number of modes in the simulations is 23, which is large enough based on our modal contribution analysis. The input central wavelengths are 1, 2, 3 and 4 μm. The first set of simulations is performed with the following parameters: The input spatio-temporal Gaussian pulse intensity is $I = 1.5\times10^{14}$ $\mathrm{Wcm^{-2}}$ with transform-limited, full width half maximum pulse duration ($\tau_p$) of 100 fs and $1/e^2$ beam radius ($w$) of $0.645a_0$ with $a_0$ =200 μm, which provides optimal coupling into a capillary. We maintain the same input intensity/energy for all the wavelengths, which means that the input powers in terms of critical power are different for different wavelengths: $2.5P_{cr}$, $0.63P_{cr}$, $0.28P_{cr}$ and $0.16P_{cr}$ for $\lambda$ = 1, 2, 3 and 4 μm, respectively. The zero dispersion wavelength for the fundamental mode occurs at $\lambda$ = 1.24 μm and therefore, all the considered wavelengths belong to the anomalous group-velocity dispersion (GVD) regime except $\lambda$ = 1 μm. The dispersion lengths of the fundamental mode in Ar-filled capillaries for $\tau_p$ =100 fs are 565 m, 112 m, 29 m and 12 m for $\lambda$ = 1, 2, 3 and 4 μm, respectively, which are much longer than the simulated propagation distance (5 cm). We also perform simulations with different capillary radii, laser intensities, pressure, pulse-width and Ne gas and discuss the results in Sec. 4.

## 3. Results and discussion

The evolution of peak intensities and plasma densities (global maxima) as a function of propagation distance are shown in Fig. 1 for $\lambda$ = 1 μm (red solid line), 2 μm (black dashed line), 3 μm (magenta dotted line) and 4 μm (blue dashed-dotted line). Since the input intensities and wavelengths belong to the tunneling ionization regime, plasma densities are similar ($\sim 10^{18}$ $\mathrm{cm^{-3}}$) at the capillary input. As shown, plasma defocuses laser pulses resulting in lower intensities for all the wavelengths. However, the pulse for $\lambda$ = 1 μm quickly recovers from plasma defocusing and reaches high intensities again as it propagates. This can be explained by two mechanisms: It is due to 1) less plasma defocusing at shorter wavelengths for a given plasma density and 2) larger optical Kerr effect at shorter wavelengths induced by higher input power in terms of $P_{cr}$. As a comparison, the 2-μm and 3-μm pulses exhibit intensity increase later (e.g., at $z \simeq 4$ cm for $\lambda$ = 2 μm and at $z \simeq 3$ and 4 cm for $\lambda$ = 3 μm), which is due to spatio-temporal reshaping which will be discussed soon. In contrast, although intensity increase occurs at $z \simeq 2$ cm for $\lambda$ = 4 μm, it is not strong compared with $\lambda$ = 2 and 3 μm.

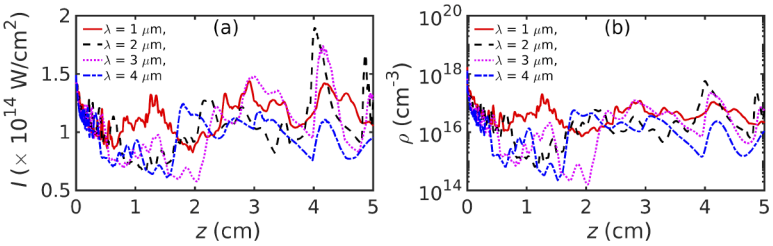


**Fig. 1.** (a) Peak intensities and (b) peak plasma densities versus propagation distance for $\lambda$ = 1 μm (red solid line), 2 μm (black dashed line), 3 μm (magenta dotted line) and 4 μm (blue dashed-dotted line).

Optics EXPRESS

In our simulations, we find that the spatio-temporal dynamics change drastically for different wavelengths even with the same input intensity as shown in Fig. 2 (see Visualization 1, Visualization 2, Visualization 3 and Visualization 4). Here each spatio-temporal profile is proportional to the square of the carrier-resolved electric field and its envelope represents the laser intensity. It is evident that when ionization occurs, intensities at the trailing parts decrease due to plasma defocusing [Fig. 2(a,e,i,m)], which results in pulse self-compression near the capillary input. However, for further propagation, the trailing parts of the pulses start to exhibit on-axis ($r = 0$) high intensities for some wavelengths [see Fig. 2(h) for 2 μm, Fig. 2(k) for 3 μm and Fig. 2(o) for 4 μm]. Since the input powers are less than $P_{cr}$ for $\lambda = 2$, 3 and 4 μm, it is not clear whether this intensity increase at later times occurs due to Kerr-induced self-focusing. Therefore, we perform additional calculations by removing the optical Kerr effect ($n_2I$), which shows that the intensity increase still occurs even without $n_2I$. For instance, Fig. 3 shows the spatio-temporal profiles with (a) and without (b) $n_2I$ for $\lambda = 4$ μm at $z$ =2.8 cm, which shows similar trailing pulses. We think that these trailing pulses are mainly due to excitation of higher-order modes via plasma. The role of $n_2I$ in pulse self-compression is discussed later. To quantify, we calculate the spectrally-integrated contribution from each mode as the laser pulses propagate. Figure 4 shows the normalized modal contribution of the five lowest modes versus propagation distance for different wavelengths. For $\lambda = 1$ μm, the contribution from the fundamental mode decreases monotonically with propagation distance and reaches down to 50 % at the end of propagation. As a comparison, the contributions from the fundamental mode suddenly drop to 38 % at $z \sim$ 4 cm for $\lambda = 2$ μm and 50 % at $z \sim 3$ cm for $\lambda = 3$ μm. This excitation of higher-order modes is closely related to the peak intensity increase shown in Fig. 1(a). In contrast, the 4-μm pulse maintains almost 75 % of the total energy in the fundamental mode till the end of propagation. Excitation of higher-order modes and resulting modal interference can produce off-axis intensity maxima [see, for instance, Fig. 2(a and e)], which leads to off-axis maximum plasma generation and resulting plasma-induced focusing [60].

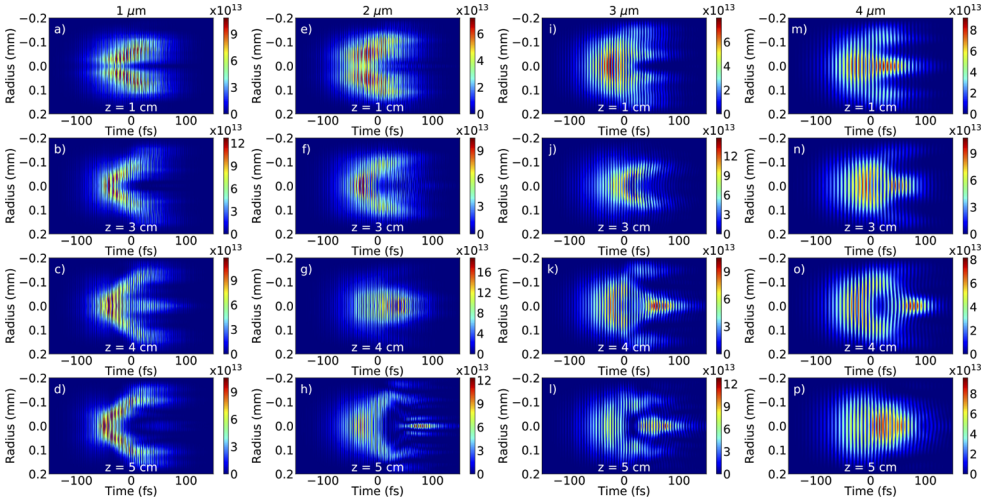


**Fig. 2.** Spatio-temporal profiles at various propagation distances for (a-d) $\lambda = 1$ μm, (e-h) $\lambda = 2$ μm, (i-l) $\lambda = 3$ μm and (m-p) $\lambda = 4$ μm. The profile is proportional to the square of the carrier-resolved electric field and its envelope represents the laser intensity. The color bars indicate intensity in $\mathrm{Wcm}^{-2}$.

We investigate the effect of higher-order modes on the pulse temporal dynamics. Figure 5 shows the on-axis temporal profiles versus propagation distance for different wavelengths. As the pulses propagate, the pulse duration for $\lambda = 1$ μm becomes the minimum ($\sim$ 28.4 fs) at $z \sim$

Optics EXPRESS

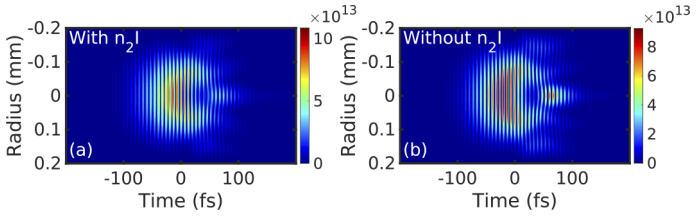


**Fig. 3.** Spatio-temporal profiles for $\lambda = 4$ μm at $z$ =2.8 cm (a) with $n_2I$ and (b) without $n_2I$. The profile is proportional to the square of the carrier-resolved electric field and its envelope represents the laser intensity. The color bars indicate intensity in $\mathrm{Wcm}^{-2}$.

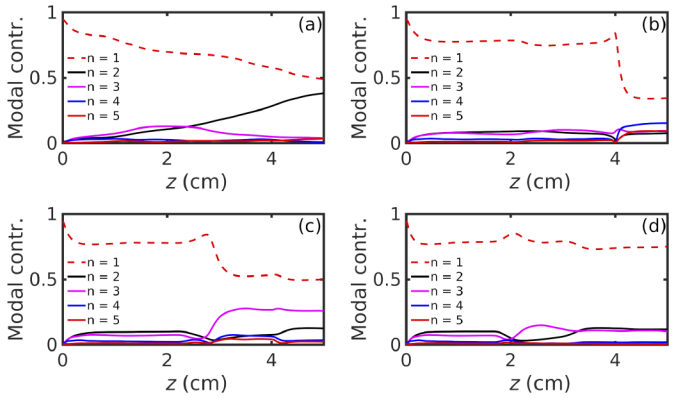


**Fig. 4.** The normalized modal contribution (Modal contr.) of the five lowest modes ($n$) versus propagation distance ($z$) for (a) $\lambda = 1$ μm, (b) $\lambda = 2$ μm, (c) $\lambda = 3$ μm and (d) $\lambda = 4$ μm.

3 cm [see Fig. 5(e)] and remains almost the same till $z \sim 4$ cm whereas pulse splitting and mainly pulse broadening occur for other wavelengths. We also perform spatially-averaged pulse duration analysis within a 100-μm diameter at $z \sim 3$ cm for $\lambda = 1$ μm, which shows compression by a factor of $\sim 2$ with 45-fs pulse duration [Fig. 5(f)]. At the end of propagation, the pulse duration for $\lambda = 1$ μm is $\sim 42.3$ fs whereas the pulse duration for $\lambda = 4$ μm increases to $\sim 118$ fs. Furthermore, to investigate the role of Kerr effect in pulse self-compression, we perform additional calculations by removing the optical Kerr effect ($n_2I$). Figure 6 shows the calculated on-axis temporal profiles versus propagation distance without $n_2I$ term. For $\lambda = 1$ μm whose input power is greater than $P_{cr}$ [Fig. 6(a)], pulse self-compression does not occur without $n_2I$ for $z \geq 3$ cm, which is in contrast to the simulation with $n_2I$ [Fig. 5(a)]. Our calculations confirm that self-focusing induced plasma is the key parameter for pulse self-compression.

To understand the pulse self-compression for $\lambda = 1$ μm and pulse broadening for other wavelengths, we investigate the group velocities of various modes. The wavelength-dependent group velocities are calculated using $[v_{g,n} = (dk_{z,n}/d\omega\ |_{\omega=\omega_0})^{-1}]$, where $k_{z,n} = \sqrt{k^2(\omega) - k_{\perp,n}^2}$ is the modal-dependent wave number. The group velocities of the four lowest modes for an Ar-filled capillary with 1 bar pressure and without plasma are shown in Fig. 7(a). To investigate the effect of plasma, we also calculate group velocities using the plasma-dependent refractive index given by $n_p(\omega) = [n(\omega) - 1](\rho_0 - \rho)/\rho_0 + 1 - \rho/2\rho_c$, where $n(\omega)$ is the neutral medium refractive index based on the Sellmeier equation, $\rho_0$ is the neutral density of Ar, $\rho$ is the plasma density, and $\rho_c$ is the critical plasma density. Here we assume a constant plasma density of 1 $\times 10^{17}$ $\mathrm{cm}^{-3}$, which is similar to our numerical simulation results [Fig. 1(b)]. Although the group

Optics EXPRESS

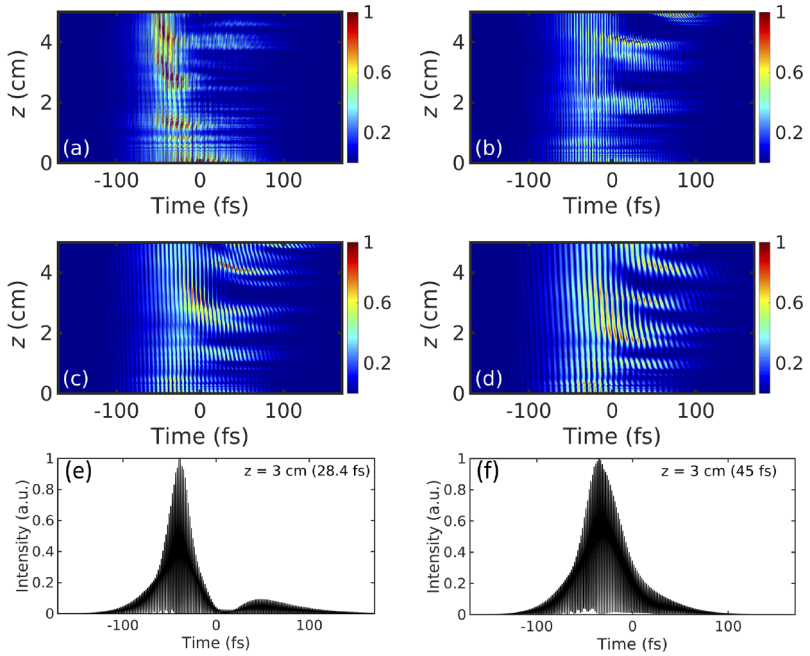


**Fig. 5.** Normalized on-axis temporal profiles versus propagation distance for (a) $\lambda = 1$ µm, (b) $\lambda = 2$ µm, (c) $\lambda = 3$ µm and (d) $\lambda = 4$ µm. The lineout of (e) on-axis and (f) spatially-averaged temporal profile at $z \sim 3$ cm, which is the position of minimum pulse duration for $\lambda = 1$ µm.

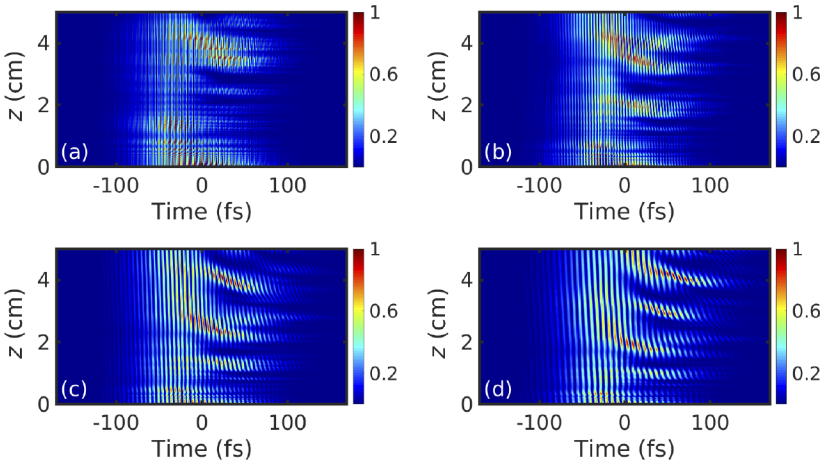


**Fig. 6.** Normalized on-axis temporal profiles versus propagation distance without $n_2 I$ for (a) $\lambda = 1$ µm, (b) $\lambda = 2$ µm, (c) $\lambda = 3$ µm and (d) $\lambda = 4$ µm.

velocities decreases with plasma as shown in Fig. 7(b), the difference between group velocities of different modes remain almost the same for our simulated wavelengths. In further detail, we calculate group velocity mismatch (GVM) between two capillary modes using Taylor expansion $k_{z,n} \sim k(\omega) - k_{\perp,n}^2/2k(\omega)$. Since $v_{g,n} = (dk_{z,n}/d\omega)^{-1} \sim (dk/d\omega)^{-1}[1 + \gamma_n^2/2a_0^2k^2(\omega)]^{-1}$, GVM

Optics EXPRESS

between two ($m^{th}$ and $n^{th}$) modes can be written as,

$$\text{GVM} = \left|\frac{1}{v_{g,m}} - \frac{1}{v_{g,n}}\right| = \left|\left(\frac{dk}{d\omega}\right)\frac{\gamma_m^2 - \gamma_n^2}{2a_0^2k^2(\omega)}\right| = \left|\left(\frac{dk}{d\omega}\right)\frac{\gamma_m^2 - \gamma_n^2}{8\pi^2n^2(\omega)}\left(\frac{\lambda^2}{a_0^2}\right)\right|. \tag{3}$$

In the above equation,

$$\frac{dk}{d\omega} = \frac{n(\omega)}{c}\left(1 - \frac{\lambda}{n(\omega)}\frac{dn}{d\lambda}\right). \tag{4}$$

However, $|\lambda dn/n(\omega)d\lambda| < 10^{-5}$ for $\lambda \geq 1$ μm and 1-bar Ar and thus GVM scales as $\lambda^2/a_0^2$. This is confirmed by Fig. 7(a) where GVM is larger at longer wavelengths, resulting in larger delays between the fundamental mode and higher-order mode at longer wavelengths. Our calculations shows that the delays between the fundamental ($n = 1$) and the $4^{th}$ mode are ~ 7, ~ 28, ~ 63, and ~ 113 fs for $\lambda = 1$, 2, 3 and 4 μm, respectively for 5-cm propagation. Likewise, the delay between the fundamental and other higher-order modes increases at longer wavelengths. This GVM analysis clearly explains the correlation between excitation of higher-order modes and pulse splitting. For example, the contributions from higher-order modes suddenly increase at $z \sim$ 4 cm for $\lambda = 2$ μm [see Fig. 4(b)] resulting in pulse elongation and eventually splitting at $z = 5$ cm [see Fig. 5(b)]. Similarly for $\lambda = 3$ μm, the contributions from higher-order modes abruptly increase at $z \sim 3$ cm [see Fig. 4(c)] and pulse splitting starts to occur at $z = 4$ cm and becomes significant at $z = 5$ cm [see Fig. 5(c)].

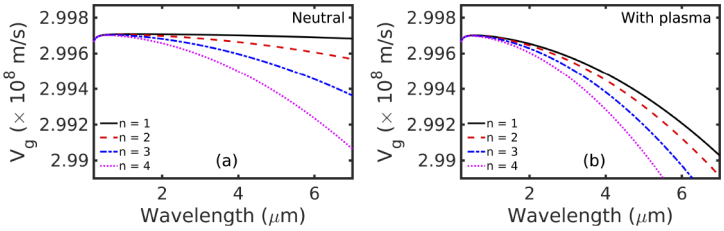


**Fig. 7.** Group velocities versus wavelength for the four lowest mode; $n = 1$ (black solid line), $n = 2$ (red dashed line), $n = 3$ (blue dashed dotted line) and $n = 4$ (magenta dotted line), (a) in neutral medium and (b) with plasma.

In addition, we calculate the time-dependent modal contributions at the positions of significant pulse splitting, for instance, at $z = 4.9$ cm for $\lambda = 2$ and 3 μm and at $z = 4.1$ cm for $\lambda = 4$ μm as shown in Fig. 8(a,c,e). Due to pulse splitting, there are two pulses: main and trailing pulses and we analyze the modal contributions in each pulse. In each pulse, we average over 50 fs in time centered at the local intensity peaks. As shown in Fig. 8(b,d,f), in the main pulses (red solid circle), the fundamental mode dominates for all three wavelengths whereas in the trailing pulses (blue solid triangle), the contributions from higher-order modes are significant. For instance, the $4^{th}$, $5^{th}$ and $6^{th}$ modes contain most of the energy in the trailing pulse for $\lambda = 2$ μm. Similarly, ~ 55 % energy is contained in the $3^{rd}$ mode for $\lambda = 3$ μm and ~ 90 % energy is contained in the $2^{nd}$ mode for $\lambda = 4$ μm. This confirms that for $\lambda = 2$, 3 and 4 μm, excited higher-order modes lag behind the fundamental mode due to smaller group velocities, which results in pulse splitting. In contrast, since GVM between modes is smaller for $\lambda = 1$ μm, higher-order modes mostly overlap with the fundamental mode temporally and thus pulse broadening and/or splitting is minimal.

Optics EXPRESS

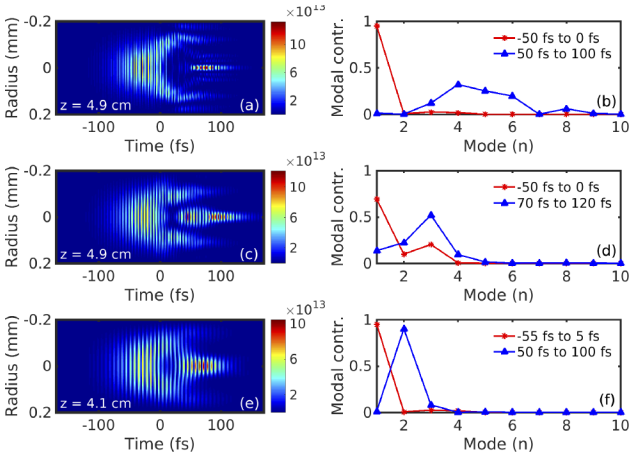


**Fig. 8.** Examples of spatio-temporal profiles at the position of pulse splitting for (a) $\lambda = 2$ μm, (b) $\lambda = 3$ μm and (c) $\lambda = 4$ μm. Modal contribution analysis for main (red solid circle) and trailing (blue solid triangle) pulses are shown for (b) $\lambda = 2$ μm, (d) $\lambda = 3$ μm and (f) $\lambda = 4$ μm.

## 4. More results

### 4.1. Capillary radius dependent pulse self-compression

We also investigate the role of capillary radius on the spatio-temporal dynamics via simulations, in particular, to confirm the $1/a_0^2$ scaling of capillary dispersion which has been discussed in previous work (see, for instance, Ref. [7,61,62]). Simulations are performed for two more radii $a_0 = 100$ μm and 250 μm with the input intensity of $I = 1.5 \times 10^{14}$ Wcm$^{-2}$. To have the same intensity for both radii, the input powers with $a_0 = 100$ μm are $0.63P_{cr}$, $0.16P_{cr}$, $0.07P_{cr}$ and $0.04P_{cr}$ for $\lambda = 1$, 2, 3 and 4 μm, respectively, and those with $a_0 = 250$ μm are $3.93P_{cr}$, $0.99P_{cr}$, $0.44P_{cr}$ and $0.25P_{cr}$ for $\lambda = 1$, 2, 3 and 4 μm, respectively. Pulse spatio-temporal dynamics, particularly pulse self-compression with $a_0 = 100$ μm is different from that with $a_0 = 200$ μm (Sec. 3). The normalized on-axis temporal profiles versus propagation distance for $a_0 = 100$ μm are shown in Fig. 9(a-d) for $\lambda = 1$, 2, 3 and 4 μm, respectively. Although pulse self-compression occurs for $\lambda = 1$ μm, it happens with pulse splitting. Overall, compared to $a_0 = 200$ μm (see Fig. 5), pulse splitting and broadening are more significant with $a_0 = 100$ μm for all the wavelengths. It is consistent with the fact that GVM is inversely proportional to the square of capillary radius (GVM $\propto \lambda^2/a_0^2$) and therefore the delays between the fundamental and higher-order modes for smaller capillary radius increase. The group velocities as a function of wavelength for the four lowest modes with $a_0 = 100$ μm are shown in Fig. 9(e), which shows larger GVM than that with $a_0 = 200$ μm shown in Fig. 7(a). For instance, the delay between the fundamental and the 4$^{th}$ mode for $\lambda = 1$ μm is ~ 7 fs with $a_0 = 200$ μm but it increases to ~ 28 fs with $a_0 = 100$ μm for 5-cm propagation resulting in pulse splitting.

Pulse self-compression with $a_0 = 250$ μm is similar to that with $a_0 = 200$ μm, as shown in Fig. 10. Pulse self-compression is still most efficient for $\lambda = 1$ μm and the minimum pulse duration is ~ 20 fs, which occurs near $z \sim 4.5$ cm. The spatially-averaged pulse duration within a 100-μm diameter is about 30 fs, yielding pulse self-compression by a factor of ~ 3.3. Furthermore, pulse splitting is less with $a_0 = 250$ μm compared to $a_0 = 100$ and 200 μm because of the smaller GVM among the modes [see Fig. 10(e)]. In summary, pulses at $\lambda = 1$ μm yield better pulse self-compression than longer wavelengths (2, 3 and 4 μm) irrespective of the capillary radius for the weak ionization regime.

Optics EXPRESS

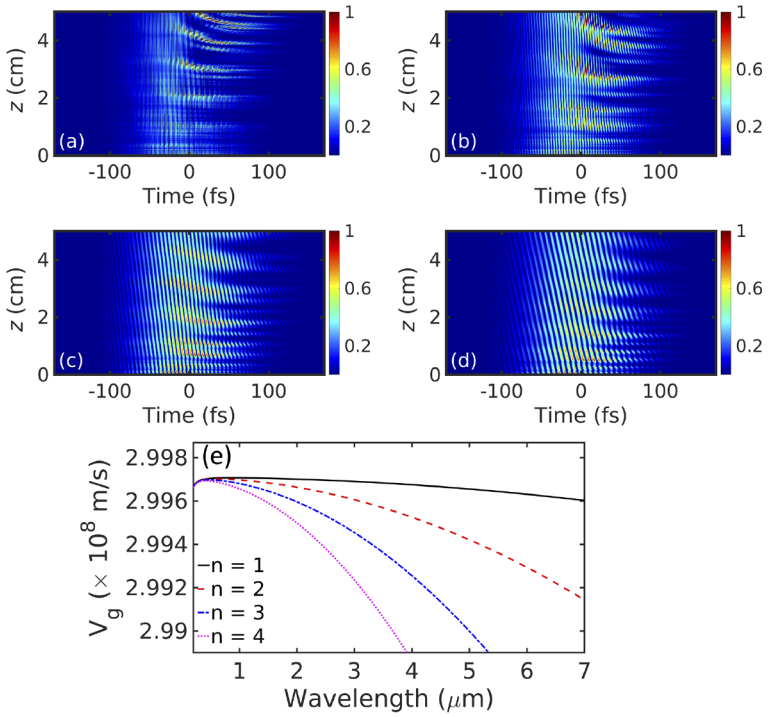


**Fig. 9.** Normalized on-axis temporal profiles versus propagation distance with $a_0$ =100 μm for (a) $\lambda$ = 1 μm, (b) $\lambda$ = 2 μm, (c) $\lambda$ = 3 μm and (d) $\lambda$ = 4 μm. (e) Group velocities versus wavelength for the four lowest modes with $a_0$ = 100 μm; n = 1 (black solid line), n = 2 (red dashed line), n = 3 (blue dashed dotted line) and n = 4 (magenta dotted line).

### 4.2. *Intensity-dependent pulse self-compression*

Since excitation of higher-order modes depends on the intensity during pulse propagation in capillaries, we also investigate the effect of the intensity. Here we show simulation results for two more intensities: $I = 1 \times 10^{14}$ Wcm$^{-2}$ and $I = 2.5 \times 10^{14}$ Wcm$^{-2}$. Note that all the previous results are at $I = 1.5 \times 10^{14}$ Wcm$^{-2}$. The peak intensities versus propagation distance for $I = 1 \times 10^{14}$ Wcm$^{-2}$ are shown in Fig. 11(a). Defocusing due to plasma occurs near the input of the capillary for all the wavelengths but due to less ionization it is not strong compared with $I = 1.5 \times 10^{14}$ Wcm$^{-2}$ [Fig. 1(a)]. The contribution from the fundamental mode versus propagation distance is shown in Fig. 11(b) for $\lambda$ = 1 μm (red solid line), 2 μm (black dashed line), 3 μm (magenta dotted line), and 4 μm (black dash-dot line). Due to low intensity and weak ionization, excitement of higher-order modes are negligible for $\lambda$ = 2, 3 and 4 μm and thus pulse broadening and/or splitting does not occur during propagation as shown in Fig. 11(c-e). However, since $P_{cr}$ scales with $\lambda^2$, the pulse for $\lambda$ = 1 μm experiences more self-focusing and thus maintains nearly constant intensities throughout the propagation, exhibiting plasma-induced self-compression even at $I = 1 \times 10^{14}$ Wcm$^{-2}$ [Fig. 11(f)]. The minimum pulse duration is ~ 32 fs which occurs near $z \sim 4.6$ cm. To confirm the role of optical Kerr effect, we perform a calculation without $n_2 I$ at $I = 1 \times 10^{14}$ Wcm$^{-2}$ for $\lambda$ = 1 μm. Comparison of normalized on-axis temporal profiles with and without $n_2 I$ is shown in Figs. 11(f) and 11(g), which shows that there is no pulse self-compression without $n_2 I$. Therefore, we conclude that the optical nonlinearities via Kerr effect and plasma are critical for pulse self-compression.

For input intensity of $I = 2.5 \times 10^{14}$ Wcm$^{-2}$, spatio-temporal dynamics are much more complex due to higher plasma density and resulting greater excitation of higher-order modes for all the

Optics EXPRESS

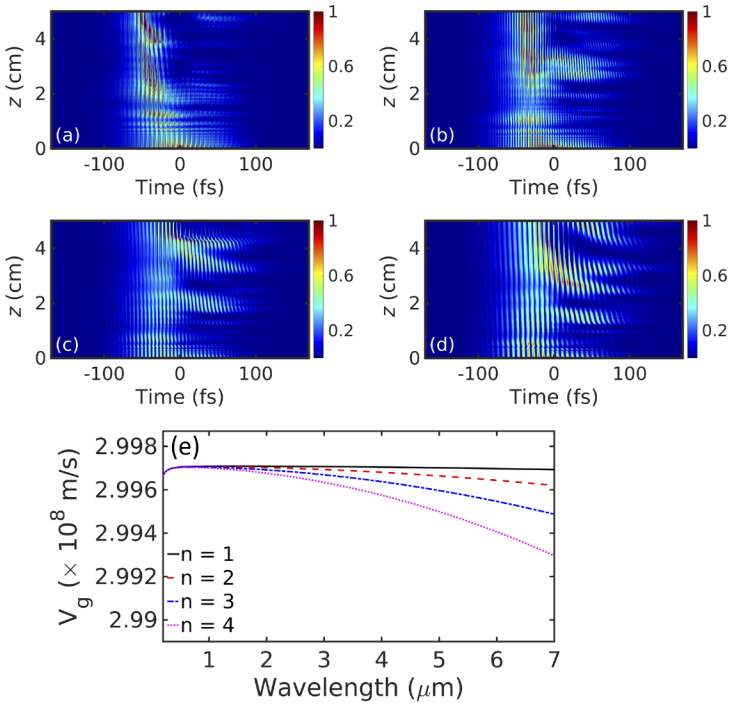


**Fig. 10.** Normalized on-axis temporal profiles versus propagation distance with $a_0$ =250 μm for (a) $\lambda$ = 1 μm, (b) $\lambda$ = 2 μm, (c) $\lambda$ = 3 μm and (d) $\lambda$ = 4 μm. (e) Group velocities versus wavelength for the four lowest modes with $a_0$ = 250 μm; n = 1 (black solid line), n = 2 (red dashed line), n = 3 (blue dashed dotted line) and n = 4 (magenta dotted line).

wavelengths. For instance with $\lambda$ = 3 μm, Fig. 12(a) shows the spatio-temporal profile at the output of the capillary and Fig. 12(b) shows the on-axis temporal evolution with propagation distance. Multiple pulse splitting occur, resulting in complex spatio-temporal profiles as shown in Fig. 12(a). Therefore, pulse self-compression in capillaries is not easy to achieve with large plasma densities (e.g., full ionization) though multiple ionization may produce self-compression under appropriate conditions [25].

### 4.3. *Pressure-dependent pulse self-compression*

We also perform simulations by varying the pressure inside the capillary. Since properties such as refractive index, gas density and nonlinearities change with pressure, it is important to optimize it for pulse self-compression. Simulations are performed for two more pressures, 0.5 bar and 2 bar with the input intensity of $I = 1.5 \times 10^{14}$ Wcm$^{-2}$ (the results in Sec. 3 are with 1 bar pressure). The normalized on-axis temporal profiles versus propagation are shown in Fig. 13(a-d) with 0.5 bar and Fig. 13(e-f) with 2 bar for $\lambda$ = 1, 2, 3 and 4 μm, respectively. As shown in Fig. 13(a-d), pulse self-compression is still most efficient for $\lambda$ = 1 μm. However, it is not efficient as with 1 bar, compression down to ~ 50 fs at the end of the capillary. For $\lambda$ = 2, 3 and 4 μm with 0.5 bar, pulse-splitting is less pronounced compared with 1 bar because of smaller nonlinearities at lower pressure and resulting less excitation of higher-order modes. In contrast, with 2 bar, the pulse self-compresses down to ~ 18 fs near $z$ ~ 3.5 cm for $\lambda$ = μm but with more pulse-splitting. For $\lambda$ = 2, 3 and 4 μm with 2 bar, pulse-splitting is more pronounced because of greater excitation of higher-order modes and GVM among capillary modes.

Optics EXPRESS

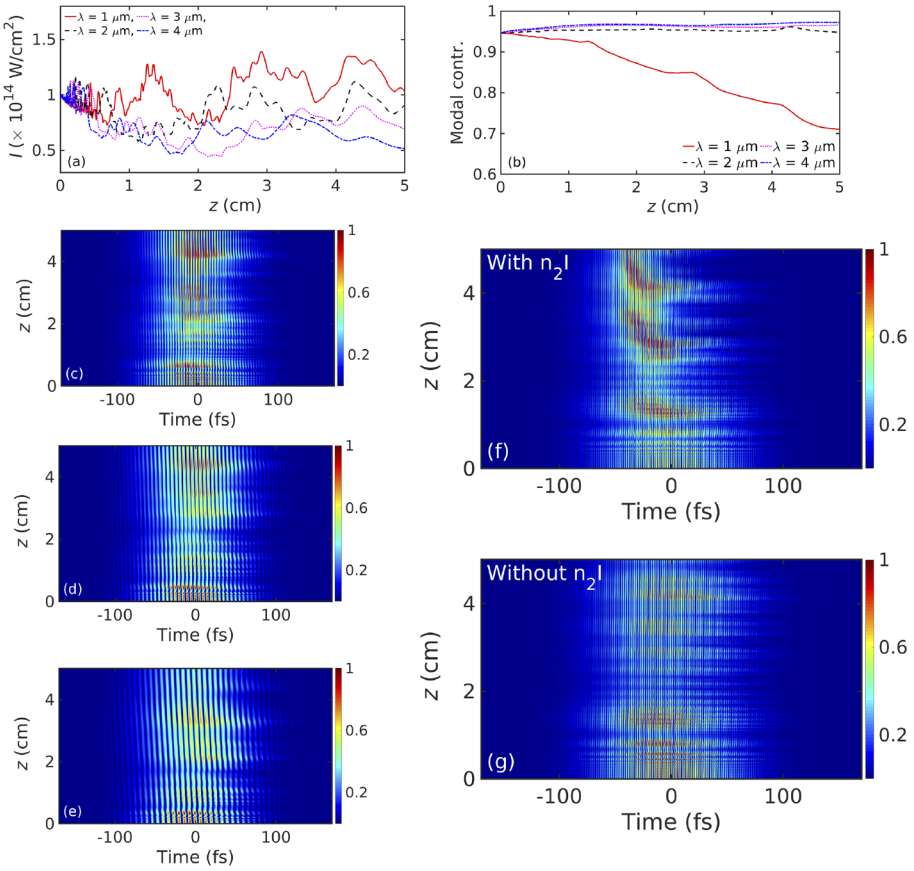


**Fig. 11.** Simulation results with $I = 1 \times 10^{14}$ Wcm$^{-2}$: (a) Peak intensity, (b) fundamental mode contribution versus propagation distance for $\lambda = 1$ μm (red solid line), 2 μm (black dashed line), 3 μm (magenta dotted line) and 4 μm (black dash-dot line). Normalized on-axis temporal profiles versus propagation distance for (c) $\lambda = 2$ μm (d) $\lambda = 3$ μm and (e) $\lambda = 4$ μm. Normalized on-axis temporal profiles for $\lambda = 1$ μm (f) with and (g) without $n_2 I$.

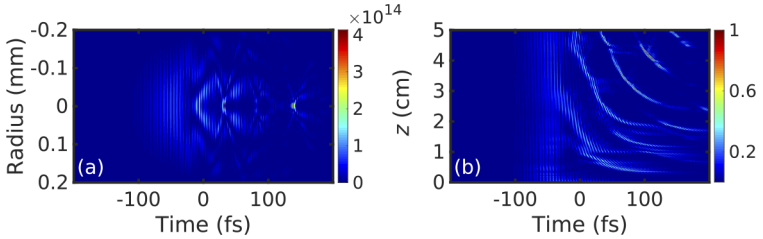


**Fig. 12.** (a) Spatio-temporal profile at the output and (b) normalized on-axis temporal profile for $\lambda = 3$ μm with input intensity of $I = 2.5 \times 10^{14}$ Wcm$^{-2}$. The color bar in (a) indicate intensity in Wcm$^{-2}$.

### 4.4. *Simulations with the same number of cycles for different wavelengths*

We perform simulations with the same number of optical cycles for all the wavelengths. We choose pulse durations of 50, 100, 150 and 200 fs for $\lambda = 1$, 2, 3 and 4 μm, respectively, with the same input intensity of $1.5 \times 10^{14}$ Wcm$^{-2}$. To have the same input intensity, we change the

Optics EXPRESS

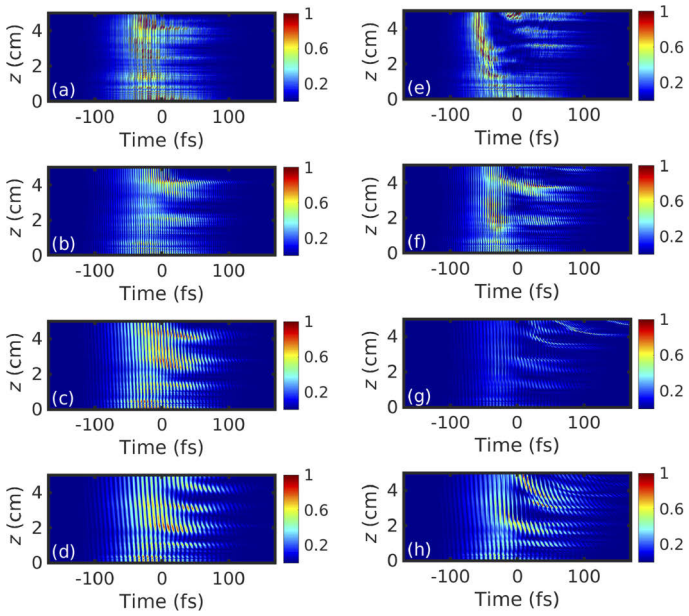


**Fig. 13.** Normalized on-axis temporal profiles versus propagation distance with 0.5 bar (left column) and 2 bar (right column) Ar pressures for (a,e) $\lambda = 1$ µm, (b,f) $\lambda = 2$ µm, (c,g) $\lambda = 3$ µm and (d,h) $\lambda = 4$ µm.

input powers accordingly for all the wavelengths. The normalized on-axis temporal profiles are shown in Fig. 14(a-d) for $\lambda = 1$, 2, 3 and 4 µm, respectively. Spatio-temporal dynamics with the same number of cycles are similar to those with the constant pulse duration so that pulse self-compression only occurs for $\lambda = 1$ µm.

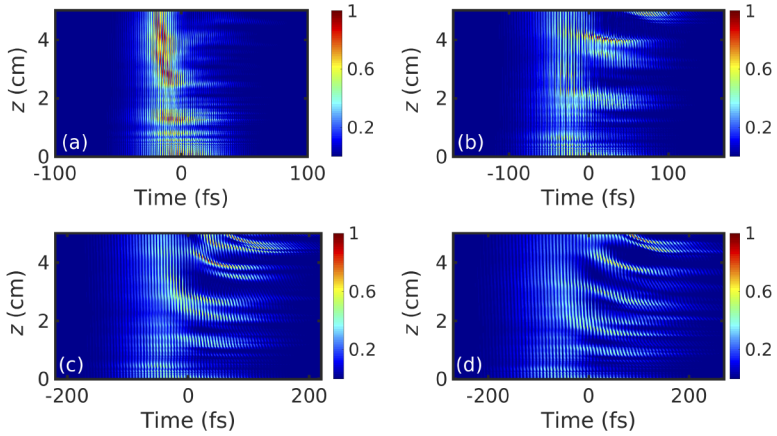


**Fig. 14.** Normalized on-axis temporal profiles versus propagation distance with the same number of cycle in a pulse for (a) $\lambda = 1$ µm, (b) $\lambda = 2$ µm, (c) $\lambda = 3$ µm and (d) $\lambda = 4$ µm. Note that x-axes are not same.

Optics EXPRESS

### 4.5. Ne-gas simulations

Since neon is another frequently-used atomic gas medium for capillary nonlinear optics, we also perform simulations with Ne-filled capillaries. The nonlinear index coefficient of Ne at 1 bar is $0.074 \times 10^{-19}$ cm$^2$W$^{-1}$ which is much smaller than that of Ar ($1 \times 10^{-19}$ cm$^2$W$^{-1}$) [63]. Since the ionization energy of Ne (21.56 eV) is higher than that of Ar (15.76 eV) [37], we use a higher input intensity at $4 \times 10^{14}$ Wcm$^{-2}$ with 100-fs pulse duration for all the wavelengths to see the plasma effects. We use the ADK ionization model [64] due to high intensity for Ne simulations. The input powers in terms of critical power are $0.52P_{cr}$, $0.13P_{cr}$, $0.058P_{cr}$ and $0.033P_{cr}$ for $\lambda$ = 1, 2, 3 and 4 μm, respectively. The evolution of peak intensities and plasma densities versus propagation distance are shown in Fig. 15(a-b). Plasma at the input quickly defocuses laser pulses resulting in intensity decrease like the Ar simulations. However, unlike Ar, only longer wavelengths reach higher intensities for further propagation [shown in Fig. 15(a)]. Since the input powers are smaller than the critical powers, these intensity increases for longer wavelengths are mainly due to complicated plasma-induced spatio-temporal localization. Most notably, in contrast to Ar, pulse self-compression does not occur for any of the wavelengths [Fig. 15(c-f)]. This comparison between Ar and Ne confirms the role of self-focusing for efficient pulse self-compression.

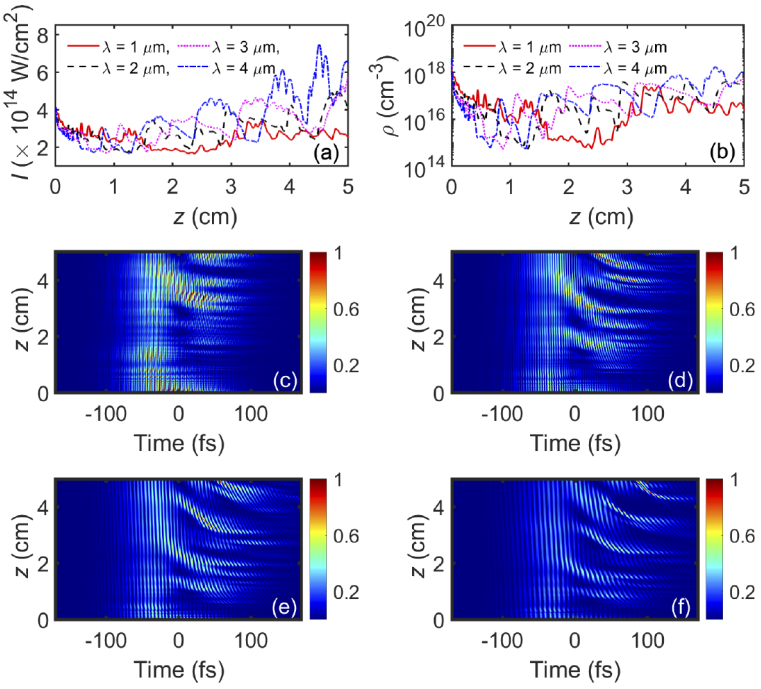


**Fig. 15.** Simulation results with Ne-filled capillaries: (a) Peak intensities and (b) peak plasma densities versus propagation distance for $\lambda$ = 1 μm (red solid line), 2 μm (black dashed line), 3 μm (magenta dotted line) and 4 μm (blue dashed-dotted line). Normalized on-axis temporal profiles versus propagation distance for (c) $\lambda$ = 1 μm, (d) $\lambda$ = 2 μm, (e) $\lambda$ = 3 μm and (f) $\lambda$ = 4 μm.

### 4.6. Simulations with pressure gradients

Since experimentalists sometimes use pressure (density) gradients at the input and output of a capillary [1] to maximize the coupling efficiency at the input and/or minimize harmonic

Optics EXPRESS

absorption at the output, we perform additional simulations with density gradient at the input and output. The density gradient at the input is defined as, $n(z) = \sqrt{n_d^2 + (z)(n_0^2 - n_d^2)/L}$, where $n_0$ is the neutral density at 1 bar, $n_d = 0.2n_0$ is the density at the entrance, $L = 0.5$ cm is the gradient length at the input and $z$ is the propagation distance [1]. The same density gradient profile is also defined at the output so that there are 0.5-cm density gradient region at the input, 4-cm constant density region, and 0.5-cm density gradient region at the output. As shown in Fig. 16 which should be compared with Fig. 5 (without density gradient), overall there is not much difference in the pulse self-compression and temporal dynamics.

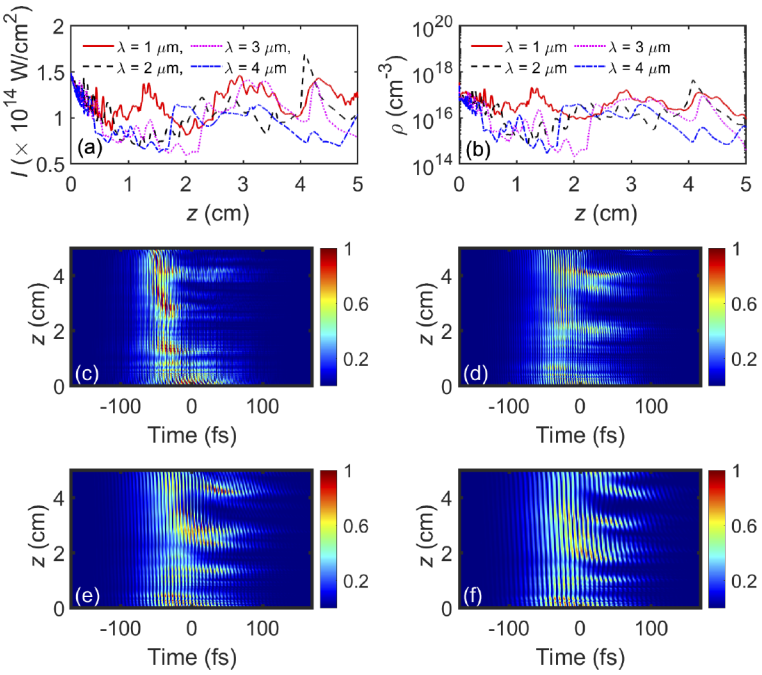


**Fig. 16.** Simulation results with pressure gradients: (a) Peak intensities and (b) peak plasma densities versus propagation distance for $\lambda = 1$ μm (red solid line), 2 μm (black dashed line), 3 μm (magenta dotted line) and 4 μm (blue dashed-dotted line). Normalized on-axis temporal profiles versus propagation distance for (c) $\lambda = 1$ μm, (d) $\lambda = 2$ μm, (e) $\lambda = 3$ μm and (f) $\lambda = 4$ μm.

### 4.7. *Simulations with the same power in terms of critical power*

As we have discussed, the optical Kerr effect plays an important role in pulse self-compression. Therefore, we perform simulations with the same laser input power in terms of critical power which scales with $\lambda^2$. The input power is $2.5P_{cr}$ with 100-fs pulse duration for all the wavelengths. We use the same input intensity ($1.5 \times 10^{14}$ Wcm$^{-2}$) for all the wavelengths and thus we use different capillary radii: 200, 400, 600, and 800 μm for $\lambda = 1$, 2, 3 and 4 μm, respectively. This is also important because GVM among different modes scales $\lambda^2/a_0^2$ [Eq. (3)] and is thus the same for all the wavelengths. The evolution of peak intensities and plasma densities versus propagation distance are shown in Fig. 17(a-b). Overall, higher intensities are maintained for shorter wavelengths. It is due to larger plasma defocusing at longer wavelengths. Note that it is not due to capillary modal loss since the loss coefficient scales with $\lambda^2/a_0^3$ and is thus smaller at longer wavelengths. The normalized on-axis temporal profiles as a function of propagation distance are shown in Fig. 17(c-f). Pulse self-compression occurs even for long wavelengths with

Optics EXPRESS

minimal pulse-splitting because of nonlinearities via plasma and optical Kerr effect as well as the same GVM among different capillary modes. These results also confirm the critical role of self-focusing for pulse self-compression. In summary, if high laser powers (energies) for plasma generation and self-focusing are available at long wavelengths, large-radius capillaries should be used for pulse self-compression for long wavelengths to minimize GVM among different capillary modes.

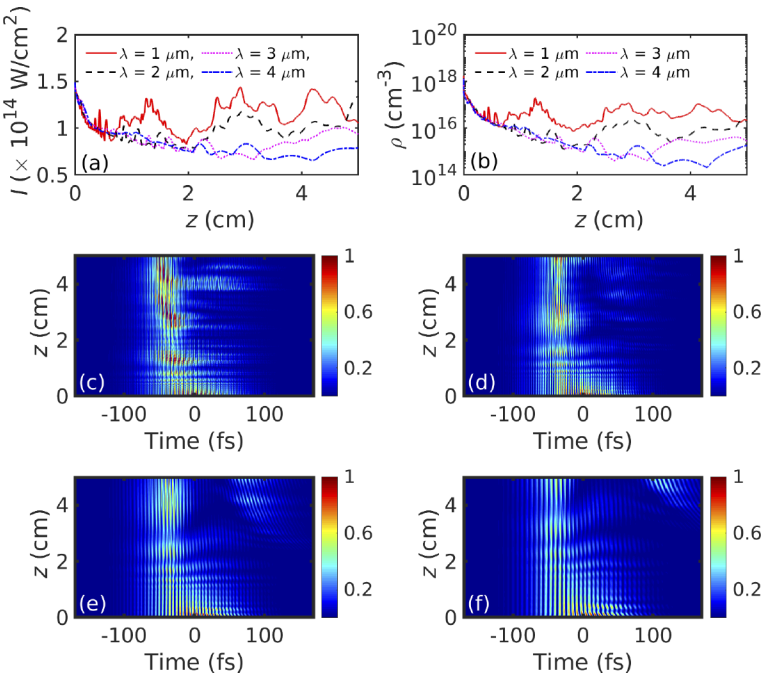


**Fig. 17.** Simulation results with the same input power in terms of critical power: (a) Peak intensities and (b) peak plasma densities versus propagation distance for $\lambda = 1$ μm (red solid line), 2 μm (black dashed line), 3 μm (magenta dotted line) and 4 μm (blue dashed-dotted line). Normalized on-axis temporal profiles versus propagation distance for (c) $\lambda = 1$ μm, (d) $\lambda = 2$ μm, (e) $\lambda = 3$ μm and (f) $\lambda = 4$ μm.

## 5. Conclusion

In summary, we numerically study the wavelength-dependent dynamics of high intensity femtosecond pulse propagation in gas-filled capillaries by solving the carrier-resolved unidirectional pulse propagation equation. Our simulations reveal complex spatio-temporal dynamics such as plasma-defocusing, excitement of higher-order modes and self-focusing. It is shown that pulse self-compression due to plasma is more efficient for $\lambda = 1$ μm compared to longer wavelengths ($\lambda = 2$, 3 and 4 μm) for the weak ionization regime in which nonlinear optics experiments such as HHG are frequently performed. Our finding is explained by the wavelength dependence of group velocity mismatch among capillary modes which is proportional to the square of wavelength. We also examine the role of capillary radius for pulse self-compression since group velocity mismatch is inversely proportional to the square of capillary radius. Furthermore, we investigate the intensity dependence of pulse self-compression, revealing that shorter wavelengths can exhibit self-compression even at low intensities because of self-focusing-induced plasma. At high intensities, spatio-temporal dynamics are much more complex due to greater contributions from higher-order modes. We also investigate the effect of parameters such as pressure, pulse-width

Optics EXPRESS

and Ne gas on pulse self-compression, which confirms that pulse self-compression is more efficient for shorter wavelengths. Furthermore, for pulse self-compression with long wavelengths, we find that large input pulse powers and capillary radii are required for long wavelengths to enhance self-focusing induced plasma effects and minimize GVM among different modes.

**Funding.** National Science Foundation (PHY-2010365); Air Force Office of Scientific Research (FA9550-18-1-0223).

**Acknowledgement.** The authors acknowledge useful discussion with Xiaohui Gao.

**Disclosures.** The authors declare that there are no conflicts of interest related to this article.

**Data availability.** Data underlying the results presented in this paper are not publicly available at this time but may be obtained from the authors upon reasonable request.

## References

1. T. Popmintchev, M.-C. Chen, D. Popmintchev, P. Arpin, S. Brown, S. Alisauskas, G. Andriukaitis, T. Balciunas, O. D. Mucke, A. Pugzlys, A. Baltuska, B. Shim, S. E. Schrauth, A. Gaeta, C. Hernandez-Garcia, L. Plaja, A. Becker, A. Jaron-Becker, M. M. Murnane, and H. C. Kapteyn, "Bright Coherent Ultrahigh Harmonics in the keV X-ray Regime from Mid-Infrared Femtosecond Lasers," Science **336**(6086), 1287–1291 (2012).
2. K. Krupa, A. Tonello, A. Barthélémy, T. Mansuryan, V. Couderc, G. Millot, P. Grelu, D. Modotto, S. A. Babin, and S. Wabnitz, "Multimode nonlinear fiber optics, a spatiotemporal avenue," APL Photonics **4**(11), 110901 (2019).
3. L. G. Wright and F. W. Wise, "Exotic waves in multimode hollow-core fibres," Nat. Photonics **14**(12), 713–714 (2020).
4. B. Malomed, L. Torner, F. Wise, and D. Mihalache, "On multidimensional solitons and their legacy in contemporary Atomic, Molecular and Optical physics," J. Phys. B: At., Mol. Opt. Phys. **49**(17), 170502 (2016).
5. Y. V. Kartashov, G. E. Astrakharchik, B. A. Malomed, and L. Torner, "Frontiers in multidimensional self-trapping of nonlinear fields and matter," Nat. Rev. Phys. **1**(3), 185–197 (2019).
6. R. Safaei, G. Fan, O. Kwon, K. Légaré, P. Lassonde, B. E. Schmidt, H. Ibrahim, and F. Légaré, "High-energy multidimensional solitary states in hollow-core fibres," Nat. Photonics **14**(12), 733–739 (2020).
7. J. C. Travers, T. F. Grigorova, C. Brahms, and F. Belli, "High-energy pulse self-compression and ultraviolet generation through soliton dynamics in hollow capillary fibres," Nat. Photonics **13**(8), 547–554 (2019).
8. L. G. Wright, D. N. Christodoulides, and F. W. Wise, "Spatiotemporal mode-locking in multimode fiber lasers," Science **358**(6359), 94–97 (2017).
9. R. A. Bartels, T. C. Weinacht, N. Wagner, M. Baertschy, C. H. Greene, M. M. Murnane, and H. C. Kapteyn, "Phase Modulation of Ultrashort Light Pulses using Molecular Rotational Wave Packets," Phys. Rev. Lett. **88**(1), 013903 (2001).
10. A. V. Sokolov, D. D. Yavuz, D. R. Walker, G. Y. Yin, and S. E. Harris, "Light modulation at molecular frequencies," Phys. Rev. A **63**(5), 051801 (2001).
11. M. Wittmann, A. Nazarkin, and G. Korn, "fs-pulse synthesis using phase modulation by impulsively excited molecular vibrations," Phys. Rev. Lett. **84**(24), 5508–5511 (2000).
12. P. S. J. Russell, P. Hölzer, W. Chang, A. Abdolvand, and J. C. Travers, "Hollow-core photonic crystal fibres for gas-based nonlinear optics," Nat. Photonics **8**(4), 278–286 (2014).
13. J. K. Wahlstrand, S. Zahedpour, Y.-H. Cheng, J. P. Palastro, and H. M. Milchberg, "Absolute measurement of the ultrafast nonlinear electronic and rovibrational response in H2 and D2," Phys. Rev. A **92**(6), 063828 (2015).
14. J. E. Beetar, M. Nrisimhamurty, T.-C. Truong, G. C. Nagar, Y. Liu, J. Nesper, O. Suarez, F. Rivas, Y. Wu, B. Shim, and M. Chini, "Multioctave supercontinuum generation and frequency conversion based on rotational nonlinearity," Sci. Adv. **6**(34), eabb5375 (2020).
15. P. A. Carpeggiani, G. Coccia, G. Fan, E. Kaksis, A. Pugžlys, A. Baltuška, R. Piccoli, Y.-G. Jeong, A. Rovere, R. Morandotti, L. Razzari, B. E. Schmidt, A. A. Voronin, and A. M. Zheltikov, "Extreme Raman red shift: ultrafast multimode nonlinear space-time dynamics, pulse compression, and broadly tunable frequency conversion," Optica **7**(10), 1349 (2020).
16. M. Nisoli, S. De Silvestri, and O. Svelto, "Generation of high energy 10 fs pulses by a new pulse compression technique," Appl. Phys. Lett. **68**(20), 2793–2795 (1996).
17. S. Bohman, A. Suda, T. Kanai, S. Yamaguchi, and K. Midorikawa, "Generation of 50 fs, 50 mJ pulses at 1 kHz using hollow-fiber pulse compression," Opt. Lett. **35**(11), 1887 (2010).
18. T. Nagy, P. Simon, and L. Veisz, "High-energy few-cycle pulses: post-compression techniques," Adv. Phys.: X **6**(1), 1845795 (2021).
19. S. A. Skobelev, A. V. Kim, and O. Willi, "Generation of high-energy few-cycle laser pulses by using the ionization-induced self-compression effect," Phys. Rev. Lett. **108**(12), 123904 (2012).
20. N. L. Wagner, E. A. Gibson, T. Popmintchev, I. P. Christov, M. M. Murnane, and H. C. Kapteyn, "Self-compression of ultrashort pulses through ionization-induced spatiotemporal reshaping," Phys. Rev. Lett. **93**(17), 173902 (2004).
21. C. Courtois, A. Couairon, B. Cros, J. R. Marquès, and G. Matthieussent, "Propagation of intense ultrashort laser pulses in a plasma filled capillary tube: Simulations and experiments," Phys. Plasmas **8**(7), 3445–3456 (2001).

Optics EXPRESS


22. T. J. Butcher, P. N. Anderson, R. T. Chapman, P. Horak, J. G. Frey, and W. S. Brocklesby, "Bright extreme-ultraviolet high-order-harmonic radiation from optimized pulse compression in short hollow waveguides," Phys. Rev. A **87**(4), 043822 (2013).
23. P. N. Anderson, P. Horak, J. G. Frey, and W. S. Brocklesby, "High-energy laser-pulse self-compression in short gas-filled fibers," Phys. Rev. A **89**(1), 013819 (2014).
24. B. A. López-Zubieta, E. C. Jarque, Ã. J. Sola, and J. S. Roman, "Theoretical analysis of single-cycle self-compression of near infrared pulses using high-spatial modes in capillary fibers," Opt. Express **26**(5), 6345 (2018).
25. X. Gao, G. Patwardhan, B. Shim, T. Popmintchev, H. C. Kapteyn, M. M. Murnane, and A. L. Gaeta, "Ionization-assisted spatiotemporal localization in gas-filled capillaries," Opt. Lett. **43**(13), 3112 (2018).
26. A. V. Kim, S. F. Lirin, A. M. Sergeev, E. V. Vanin, and L. Stenflo, "Compression and frequency up-conversion of an ultrashort ionizing pulse in a plasma," Phys. Rev. A **42**(4), 2493–2495 (1990).
27. O. Shorokhov, A. Pukhov, and I. Kostyukov, "Self-Compression of Laser Pulses in Plasma," Phys. Rev. Lett. **91**(26), 265002 (2003).
28. C. P. Hauri, A. Guandalini, P. Eckle, W. Kornelis, J. Biegert, and U. Keller, "Generation of intense few-cycle laser pulses through filamentation - parameter dependence," Opt. Express **13**(19), 7541 (2005).
29. G. Stibenz, N. Zhavoronkov, and G. Steinmeyer, "Self-compression of millijoule pulses to 7.8 fs duration in a white-light filament," Opt. Lett. **31**(2), 274 (2006).
30. A. A. Voronin, Y. Nomura, H. Shirai, T. Fuji, and A. Zheltikov, "Half-cycle pulses in the mid-infrared from a two-color laser-induced filament," Appl. Phys. B **117**(2), 611–619 (2014).
31. L. Gallmann, T. Pfeifer, P. Nagel, M. Abel, D. Neumark, and S. Leone, "Comparison of the filamentation and the hollow-core fiber characteristics for pulse compression into the few-cycle regime," Appl. Phys. B **86**(4), 561–566 (2007).
32. A. Braun, G. Korn, X. Liu, D. Du, J. Squier, and G. Mourou, "Self-channeling of high-peak-power femtosecond laser pulses in air," Opt. Lett. **20**(1), 73 (1995).
33. P. Sprangle, J. R. Peñano, and B. Hafizi, "Propagation of intense short laser pulses in the atmosphere," Phys. Rev. E **66**(4), 046418 (2002).
34. A. L. Gaeta, "OPTICS: Collapsing Light Really Shines," Science **301**(5629), 54–55 (2003).
35. J. R. Peñano, P. Sprangle, B. Hafizi, A. Ting, D. F. Gordon, and C. A. Kapetanakos, "Propagation of ultra-short, intense laser pulses in air," Phys. Plasmas **11**(5), 2865–2874 (2004).
36. S. L. Chin, S. A. Hosseini, W. Liu, Q. Luo, F. Théberge, N. Aközbek, A. Becker, V. P. Kandidov, O. G. Kosareva, and H. Schroeder, "The propagation of powerful femtosecond laser pulses in opticalmedia: physics, applications, and new challenges," Can. J. Phys. **83**(9), 863–905 (2005).
37. A. Couairon and A. Mysyrowicz, "Femtosecond filamentation in transparent media," Phys. Rep. **441**(2-4), 47–189 (2007).
38. L. Bergé, S. Skupin, R. Nuter, J. Kasparian, and J.-P. Wolf, "Ultrashort filaments of light in weakly ionized, optically transparent media," Rep. Prog. Phys. **70**(10), 1633–1713 (2007).
39. J. Kasparian and J.-P. Wolf, "Physics and applications of atmospheric nonlinear optics and filamentation," Opt. Express **16**(1), 466 (2008).
40. S. L. Chin, T. J. Wang, C. Marceau, J. Wu, J. S. Liu, O. Kosareva, N. Panov, Y. P. Chen, J. F. Daigle, S. Yuan, A. Azarm, W. W. Liu, T. Seideman, H. P. Zeng, M. Richardson, R. Li, and Z. Z. Xu, "Advances in intense femtosecond laser filamentation in air," Laser Phys. **22**(1), 1–53 (2012).
41. M. Kolesik and J. V. Moloney, "Modeling and simulation techniques in extreme nonlinear optics of gaseous and condensed media," Rep. Prog. Phys. **77**(1), 016401 (2014).
42. H. M. Milchberg, Y.-H. Chen, Y.-H. Cheng, N. Jhajj, J. P. Palastro, E. W. Rosenthal, S. Varma, J. K. Wahlstrand, and S. Zahedpour, "The extreme nonlinear optics of gases and femtosecond optical filamentationa)," Phys. Plasmas **21**(10), 100901 (2014).
43. D. Kartashov, S. Ališauskas, A. Pugžlys, A. Voronin, A. Zheltikov, M. Petrarca, P. Béjot, J. Kasparian, J.-P. Wolf, and A. Baltuška, "White light generation over three octaves by femtosecond filament at 3.9 um in argon," Opt. Lett. **37**(16), 3456–3458 (2012).
44. L. Bergé, J. Rolle, and C. Köhler, "Enhanced self-compression of mid-infrared laser filaments in argon," Phys. Rev. A **88**(2), 023816 (2013).
45. A. V. Mitrofanov, A. A. Voronin, D. A. Sidorov-Biryukov, A. Pugžlys, E. A. Stepanov, G. Andriukaitis, T. Flöry, S. Ališauskas, A. B. Fedotov, A. Baltuška, and A. M. Zheltikov, "Mid-infrared laser filaments in the atmosphere," Sci. Rep. **5**(1), 8368 (2015).
46. P. Panagiotopoulos, P. Whalen, M. Kolesik, and J. V. Moloney, "Super high power mid-infrared femtosecond light bullet," Nat. Photonics **9**(8), 543–548 (2015).
47. H. Liang, D. L. Weerawarne, P. Krogen, R. I. Grynko, C.-J. Lai, B. Shim, F. X. Kärtner, and K.-H. Hong, "Mid-infrared laser filaments in air at a kilohertz repetition rate," Optica **3**(7), 678 (2016).
48. V. Shumakova, P. Malevich, S. Ališauskas, A. Voronin, A. M. Zheltikov, D. Faccio, D. Kartashov, A. Baltuška, and A. Pugžlys, "Multi-millijoule few-cycle mid-infrared pulses through nonlinear self-compression in bulk," Nat. Commun. **7**(1), 12877 (2016).
49. Y. E. Geints and A. A. Zemlyanov, "Near- and mid-IR ultrashort laser pulse filamentation in a molecular atmosphere: a comparative analysis," Appl. Opt. **56**(5), 1397 (2017).

Optics EXPRESS


50. R. I. Grynko, G. C. Nagar, and B. Shim, "Wavelength-scaled laser filamentation in solids and plasma-assisted subcycle light-bullet generation in the long-wavelength infrared," Phys. Rev. A **98**(2), 023844 (2018).
51. S. Tochitsky, E. Welch, M. Polyanskiy, I. Pogorelsky, P. Panagiotopoulos, M. Kolesik, E. M. Wright, S. W. Koch, J. V. Moloney, J. Pigeon, and C. Joshi, "Megafilament in air formed by self-guided terawatt long-wavelength infrared laser," Nat. Photonics **13**(1), 41–46 (2019).
52. G. C. Nagar, D. Dempsey, and B. Shim, "Wavelength scaling of electron collision time in plasma for strong field laser-matter interactions in solids," Commun. Phys. **4**(1), 96 (2021).
53. A. Couairon, E. Brambilla, T. Corti, D. Majus, O. de J. Ramírez-Góngora, and M. Kolesik, "Practitioners guide to laser pulse propagation models and simulation," Eur. Phys. J. Spec. Top. **199**(1), 5–76 (2011).
54. F. Poletti and P. Horak, "Description of ultrashort pulse propagation in multimode optical fibers," J. Opt. Soc. Am. B **25**(10), 1645 (2008).
55. L. G. Wright, W. H. Renninger, D. N. Christodoulides, and F. W. Wise, "Spatiotemporal dynamics of multimode optical solitons," Opt. Express **23**(3), 3492 (2015).
56. C. Brahms, F. Belli, J. C. Travers, and P. Béjot, "Multimodal unidirectional pulse propagation equation," Phys. Rev. E **99**(3), 032217 (2019).
57. A. Börzsönyi, Z. Heiner, M. P. Kalashnikov, A. P. Kovács, and K. Osvay, "Dispersion measurement of inert gases and gas mixtures at 800 nm," Appl. Opt. **47**(27), 4856–4863 (2008).
58. E. A. J. Marcatili and R. A. Schmeltzer, "Hollow Metallic and Dielectric Waveguides for Long Distance Optical Transmission and Lasers," Bell Syst. Tech. J. **43**(4), 1783–1809 (1964).
59. A. Perelomov, V. Popov, and M. Terent'ev, "Ionization of Atoms in an Alternating Electric Field," JETP **50**, 1393 (1966).
60. X. Gao, G. Patwardhan, B. Shim, and A. L. Gaeta, "Ionization-assisted refocusing of femtosecond Gaussian beams," Opt. Lett. **44**(23), 5888 (2019).
61. A. Rundquist, C. G. Durfee, Z. Chang, C. Herne, S. Backus, M. M. Murnane, and H. C. Kapteyn, "Phase-matched generation of coherent soft x-rays," Science **280**(5368), 1412–1415 (1998).
62. T. Popmintchev, M.-C. Chen, A. Bahabad, M. Gerrity, P. Sidorenko, O. Cohen, I. P. Christov, M. M. Murnane, and H. C. Kapteyn, "Phase matching of high harmonic generation in the soft and hard X-ray regions of the spectrum," Proc. Natl. Acad. Sci. **106**(26), 10516–10521 (2009).
63. C. Bree, A. Demircan, and G. Steinmeyer, "Method for Computing the Nonlinear Refractive Index via Keldysh Theory," IEEE J. Quantum Electron. **46**(4), 433–437 (2010).
64. M. V. Ammosov, N. B. Delone, and V. P. Krainov, "Tunnel ionization of complex atoms and atomic ions in an electromagnetic field," Sov. Phys. JETP **64**, 1191–1196 (1986).